The Evolution of Concentration and Velocity Fluctuations in the Richtmyer-Meshkov Instability

D. Reese, C. Noble, A. Ames, J. Oakley, D. Rothamer, and R. Bonazza

Abstract The Richtmyer-Meshkov instability (RMI) is studied experimentally in the Wisconsin Shock Tube Laboratory (WiSTL) using a broadband, shear layer initial condition at the interface between a helium-acetone mixture and argon. This interface (Atwood number $A = 0.7$) is accelerated by either a $M = 1.6$ or $M = 2.2$ planar shock wave, and the development of the RMI is investigated through simultaneous planar laser-induced fluorescence (PLIF) and particle image velocimetry (PIV) measurements at the initial condition and four post-shock times. Simultaneously measuring concentration and velocity allows us, for the first time, to experimentally determine turbulence quantities in this regime, such as the Reynolds stresses, as well as study the effect of incident shock strength on turbulent mass-flux velocities, and the evolution of the planar turbulent kinetic energy (TKE) spectrum.

1 Introduction

The Richtmyer-Meshkov instability (RMI) [1, 2] occurs when a shock wave passes through the interface between two fluids of different density. The resulting motion is governed by the vorticity transport equation,

$$\frac{D\boldsymbol{\omega}}{Dt} = (\boldsymbol{\omega} \cdot \nabla)\,\mathbf{V} - \boldsymbol{\omega}\,(\nabla \cdot \mathbf{V}) + \nu\nabla^2\boldsymbol{\omega} + \frac{1}{\rho^2}\,(\nabla\rho \times \nabla p)\,, \tag{1}$$

where ρ is the density, p is the pressure, ν is the viscosity, $\mathbf{V} \equiv (u,v,w)$ is the velocity vector, and $\boldsymbol{\omega} \equiv \nabla \times \mathbf{V}$ is the vorticity. Upon interaction of the shock wave with the interface, vorticity is generated by the $\nabla\rho \times \nabla p$ term consequent to the misalignment of the density and pressure gradients associated with the interface and the shock wave, respectively. The macroscopic effect on the interface is the growth of any perturbations initially present on it. The current work aims to better

understand shock-induced turbulent mixing by performing shock tube experiments characterizing the RMI in a shock-accelerated shear layer. These experiments allow for concentration and velocity to be obtained at the initial condition (IC) and four post-shock times (PS1-PS4) using simultaneous planar laser-induced fluorescence (PLIF) and particle image velocimetry (PIV) measurements. This technique has been used previously to extract concentration and velocity from a shocked heavy gas curtain, and results were used to determine the effect of initial conditions on the ensuing turbulent mixing [3], the effects of reshock [4], and to give insight into the mixing transition of variable-density flows [5]. However, while these studies employed simultaneous PIV and PLIF measurements, the aforementioned experiments are inherently different from the present work as the gas curtain setup provides a two-interface initial condition, which was accelerated by a shock wave with a lower Mach number than used in the research outlined in this paper.

2   Experimental Setup

Experiments were conducted in the Wisconsin Shock Tube Laboratory (WiSTL). This facility is equipped with a 9.13 m, vertical shock tube comprised of a circular driver section of 47 cm diameter and a square driven section with 25.4 cm sides [6]. The two sections are initially separated by a steel diaphragm, which is burst by overpressurizing the driver, creating a shock wave. This shock wave travels downward into the driven section where it accelerates a broadband, shear layer interface. Twelve piezoelectric pressure transducers are placed along the length of the driven section and are used to collect pressure readings and trigger all data and image acquisition systems.

Creating the initial condition used in the present work is a multistep process. First, the driver and driven sections are evacuated to a pressure below 20 kPa in order to remove air and any other gas impurities from the shock tube. A gravitationally stable stagnation plane is then created by flowing a light gas (helium seeded with 7% acetone by volume) from the top of the tube and a heavy gas (pure argon) from the bottom while continuously evacuating excess gas through slots on the tube wall at the interface location. This flow is maintained for several minutes to ensure that all remaining air and impurities have been cleared from the tube. This gas pair has an Atwood number $A \equiv (\rho_2 - \rho_1)/(\rho_2 + \rho_1) = 0.7$, where ρ_1 and ρ_2 are the densities of the two gases. After the stagnation plane has stabilized, a statistically repeatable, broadband, shear layer initial condition is set up by injecting each gas through slots located on the shock tube side wall at the interface. This initial condition has been shown by Weber et al. [7] to be statistically repeatable in terms of spectral content. It also provides a reliable method of creating a membraneless interface containing a large range of scales [8].

Ultraviolet light from a XeCl excimer laser (308 nm) was formed into a sheet and used to excite the acetone present in the helium gas for planar laser-induced fluorescence (PLIF) imaging. Fluorescence from the acetone was captured on a

thermoelectrically cooled (to -55 °C) CCD camera (Andor model DV434-BU2), using a 50 mm Nikon lens (f /# $= 1.2$) with a bandpass filter centered at 470 nm with a full-width half-max of 271 nm and an ultrasteep short-pass filter only allowing passage of signal below 524 nm. This combination of filters ensured that only fluorescence signal from PLIF was captured by the Andor sensor.

For the PIV measurements, TiO_2 particles with a nominal diameter of 300 nm were seeded into both gas cross-flows used to create the initial condition shear interface and into the regions immediately above and below the interface. These particles allowed for the Mie scattering of the second harmonic output (532 nm) of a dual-head, flashlamp-pumped Nd:YAG laser (Ekspla model NL303D). Using a series of optics, a laser sheet was formed for use in planar laser imaging and allowed for cameras to capture particle images with a $\sim 20 \times 25$ cm field of view. Post-shock image pairs were captured with a 29 MP interline transfer CCD camera (TSI inc. model 630,094) using a 4 μs inter-frame time, while initial condition image pairs were taken with the same camera, but used an inter-frame time of 1 ms. The inter-frame times were chosen to compensate for the vastly different interface velocity fluctuations before and after acceleration by the shock wave. These timings also allowed for the final search box used in PIV to be reduced in order to obtain a large number of velocity vectors, yielding finer spatial resolution of velocity while maintaining sufficient displacement of the particles.

3   Data Processing

For both PIV and PLIF results, the first step of processing data involved subtracting the background signal. Background images were obtained by averaging the signal obtained from ten images containing laser flashes, but with no acetone or particles in the field of view. PLIF images of fluorescence signal were then processed to reveal the light-gas mole fraction by accounting for the divergent laser sheet, Beer's law attenuation, and the nonuniform laser profile. Prior to extracting velocity from PIV image data, the background-subtracted experimental particle image pairs were first corrected for intensity differences between the first and second image in each pair by conducting a normalization of the signal in each image. These normalized, background-subtracted image pairs were then used as input to the PIV algorithm.

The spatial correlation analysis of the experimental particle image pairs was completed using the Insight 4G PIV software package from TSI Inc. This method of velocimetry only allows for the calculation of velocities perpendicular to the line-of-sight of the camera, and so the velocity component in the third direction remains unknown. The chosen correlator employed a recursive rectangular grid beginning with a 128×128 pixel search box and ending with a final search box size of 32×32 pixels. The maximum displacement allowed for the interrogation search area was limited to 25% of the search box size, and the final search box size was chosen such that at least ten particles were present in each of the interrogation regions within the mixing layer in order to ensure a high valid detection probability

[9]. A zero pad mask was chosen as the spot mask engine to compute the average pixel intensity of each search box and subtract it from each pixel. Once the spot mean intensity had been subtracted from each search box, a direct correlation engine was used to perform cross-correlations where the correlation map is adjusted by an autocorrelation factor to increase the displacement measurement accuracy.

4 Experimental Results

4.1 Turbulent Mass-Flux Velocities

The first step in calculating turbulence quantities is to determine the gas density within the turbulent mixing zone. As the PLIF signal images have already been processed to show mole fraction (as discussed in Sect. 3 above), we can use this measurement to estimate the density field from

$$\rho = \rho_2' + \left(\rho_1' - \rho_2'\right)\xi, \tag{2}$$

where $\rho_1' = 0.69$ kg/m^3 and $\rho_2' = 3.48$ kg/m^3 are the post-shock densities of the light and heavy gases for the low Mach number case, $\rho_1' = 1.19$ kg/m^3 and $\rho_2' = 4.79$ kg/m^3 are the post-shock densities of the light and heavy gases for the high Mach number case, and ξ is the measured mole fraction field.

With density fields now determined, the corresponding velocity fluctuation fields can be used to calculate the directional turbulent mass-flux (TMF) velocities using

$$a_i = \frac{\langle \rho' u_i' \rangle}{\langle \rho \rangle}, \tag{3}$$

where angle brackets denote spanwise averaging and primes denote spanwise variations, i.e., $\rho' = \rho - \langle \rho \rangle$.

Turbulent mass-flux velocity is a primary turbulent source term for mixing, and a_i appears as a prefactor in the production term for the turbulent kinetic energy evolution equation. Figure 1 shows how directional TMF velocity changes across the height of the interface. We see from Fig. 1a that transverse turbulent mass-flux velocity is generally positive above the interface midpoint and becomes negative below the interface midpoint, while the streamwise turbulent mass-flux velocity shown in Fig. 1b is generally negative throughout the entire interface height. Outside of the turbulent mixing zone, the TMF velocities tend toward zero both above and below the interface in each direction. We also note larger values of turbulent mass-flux velocity in both directions for the high Mach number case, indicating greater production of turbulent kinetic energy due to the larger velocities imparted by the stronger shock.
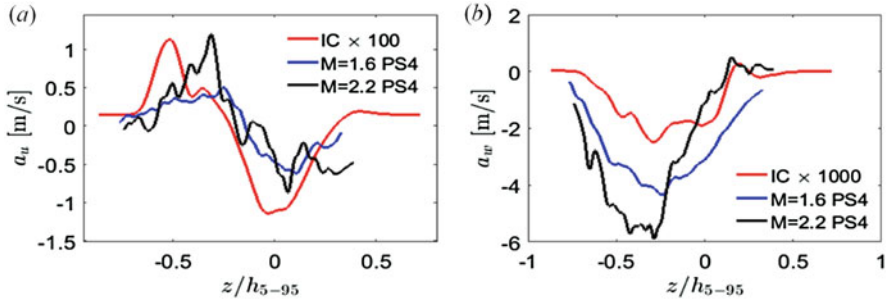
Fig. 1 Turbulent mass-flux velocity along the height of the interface in the (**a**) transverse and (**b**) streamwise directions. PS4 corresponds to $t = 3.8$ ms for $M = 1.6$ and to $t = 2.1$ ms for $M = 2.2$
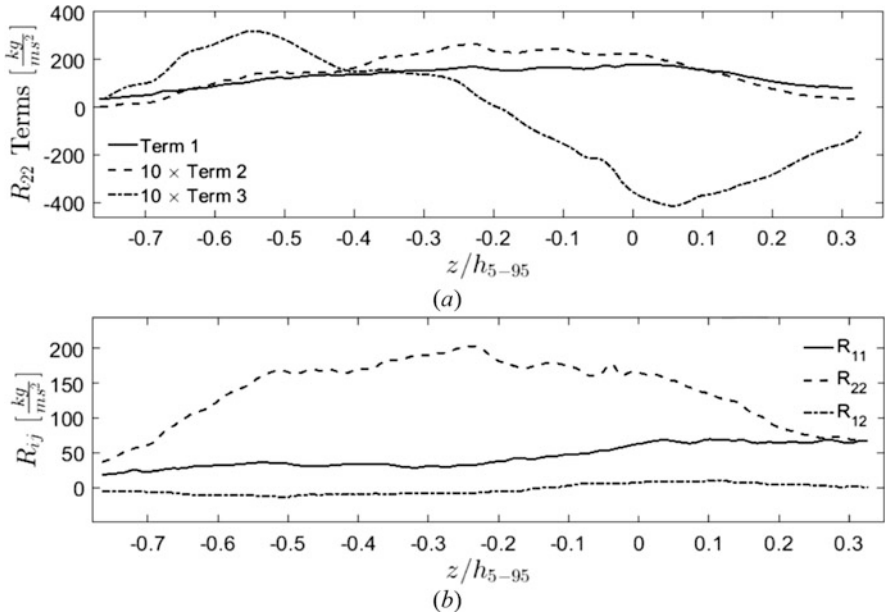
4.2 Reynolds Stresses

Reynolds stresses are the mean forces per unit area imposed on the mean flow by the turbulent fluctuations; they are defined by

$$R_{ij} = \left\langle \rho u_i^* u_j^* \right\rangle = \langle \rho \rangle \left\langle u_i' u_j' \right\rangle - \langle \rho \rangle \, a_i a_j + \left\langle \rho' u_i' u_j' \right\rangle, \tag{4}$$

where the asterisks denote Favre-averaged velocity fluctuations. In the work discussed here, three of the six components have been obtained directly through simultaneous measurements of concentration and velocity; a subscript of 1 corresponds to the transverse direction, while a subscript of 2 corresponds to the streamwise direction.

Each of the three terms on the right-hand side of the streamwise Reynolds stress component in Eq. (4) is shown individually at the latest post-shock time for the low Mach number case in Fig. 2a. Term 1 is the mean density-velocity correlation and is clearly the dominant term. Term 2 is the mass-flux term, and term 3 is the triple correlation term; both of these terms are shown to be roughly an order of magnitude smaller than the mean density-velocity correlation term. A similar trend in the importance of term 1 over the other two terms has been seen previously by Balakumar et al. [4] and Gerashchenko et al. [10].

In addition to comparing individual terms of the Reynolds stress components, the value of the components themselves can be viewed as a function of position across the turbulent mixing zone; this is shown in Fig. 2b. A comparison of the three measured components of the Reynolds stress tensor shows that the streamwise component (R_{22}) is dominant with a tendency toward zero value away from the mixing zone, indicating the greatest forces from turbulent fluctuations are occurring near the center of the mixing zone. However, the cross term remains near zero throughout much of the mixing layer, with generally negative values in the top

Fig. 2 Reynolds stress tensor results at the latest post-shock time for the low Mach number case. (**a**) Comparison of the terms of the R_{22} component of the Reynolds stress tensor and (**b**) the three measured components of the Reynolds stress tensor

portion of the layer and generally positive values in the lower portion. Finally, the transverse component of Reynolds stress lies between the two and remains positive across the turbulent mixing zone. It should be noted that these direct measurements can also be used to help constrain and validate turbulence models.

4.3 Turbulent Kinetic Energy Spectra

While density results can often be neglected when calculating the turbulent kinetic energy (TKE) of an incompressible, single-fluid flow, since the present work investigates variable-density flows which are highly compressible, it is required to consider both density and velocity when calculating the TKE spectrum. Spectra are shown at each time in the development of the instability in Fig. 3; Fig. 3a shows spectra for the low Mach number case, while Fig. 3b shows results for the high Mach number case. These spectra use an interlacing technique where the Fourier coefficient of each row is multiplied by the complex conjugate of the Fourier coefficient of the following row, which has been shown to reduce noise and extend the range of the spectrum at the highest wavenumbers. For a better comparison of the evolution of the shape of each spectrum, spectra have also been normalized by their peak value. This normalization shows a monotonic increase of energy with
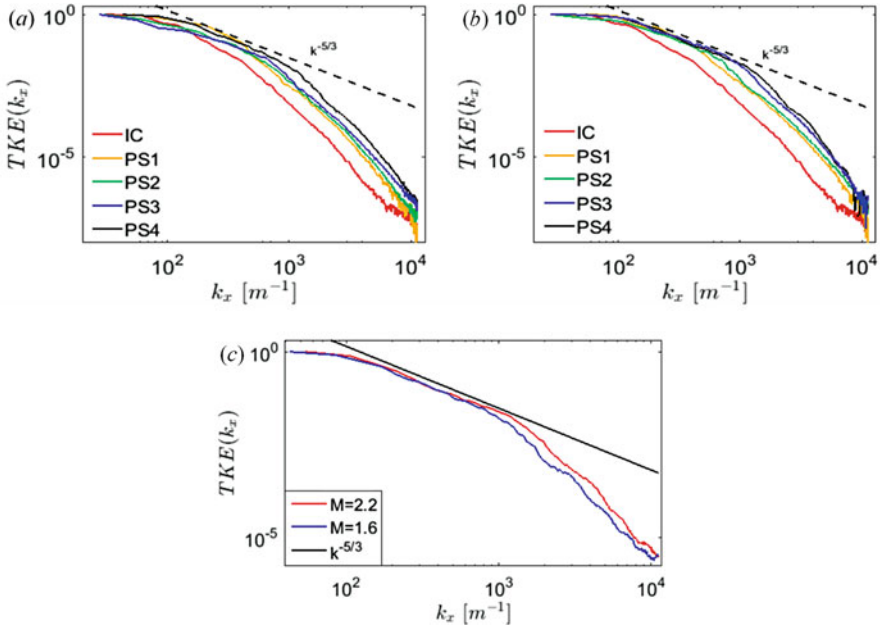
Fig. 3 Turbulent kinetic energy spectra which include the effects of both density and velocity. Evolution of spectra for the (**a**) low and (**b**) high Mach number cases. (**c**) Comparison of latest-time spectra for each case

time at the highest wavenumbers, as is expected due to the transfer of energy from production at the large scale, cascading down along the inertial range to the smaller scales as time progresses. Comparison of the latest-time spectra for each case in Fig. 3c shows that spectra tend toward a $k^{-5/3}$ slope in the inertial range by the latest time for both Mach numbers. We also note higher energy at larger wavenumbers for the higher Mach number case, as expected due to the greater energy deposited by the stronger shock.

5 Conclusions

Simultaneous PIV and PLIF experiments were conducted in a shock tube to obtain concurrent concentration and velocity field measurements. These measurements allowed, for the first time in this regime, calculations of turbulence quantities giving insight into the development of turbulence. We find that turbulent mass-flux velocities show very different behavior depending on the direction considered and vary greatly depending on position across the turbulent mixing zone. TMF velocities were also shown to be larger in magnitude by the latest time when accelerated by a stronger shock, indicating a greater production of turbulent kinetic energy, as well as a tendency toward zero value outside of the mixing layer.

Reynolds stress calculations showed that the mean density-velocity correlation term is of greatest importance when determining the mean forces per unit area imposed on the mean flow by the turbulent fluctuations, which is in agreement with results from previous work. The streamwise component of the Reynolds stress was shown to be dominant and has the largest values in the center of the mixing zone. Planar TKE spectra showed a tendency toward a $k^{-5/3}$ slope in the inertial range and a more rapid movement toward this final state for the higher Mach number case. Acceleration by a stronger shock has also been shown to increase the relative amount of energy transferred to the small scales by the latest times.

References

1. R.D. Richtmyer, Commun. Pure Appl. Math. **13**, 297 (1960)
2. E.E. Meshkov, NASA Tech. Transl. **13**, 1 (1970)
3. S. Balasubramanian, G.C. Orlicz, K.P. Prestridge, J. Turbul. **14**, 170 (2013)
4. B.J. Balakumar, G.C. Orlicz, J.R. Ristorcelli, S. Balasubramanian, K.P. Prestridge, C.D. Tomkins, J. Fluid Mech. **696**, 67–93 (2012)
5. G.C. Orlicz, S. Balasubramanian, P. Vorobieff, K.P. Prestridge, Phys. Fluids **27**, 1–23 (2015)
6. M. Anderson, B. Puranik, J. Oakley, R. Bonazza, Shock Waves **10**, 377 (2000)
7. C. Weber, *Turbulent Mixing Measurements in the Richtmyer-Meshkov Instability*, Ph.D. Thesis, University of Wisconsin-Madison, 2012
8. C. Weber, N.S. Haehn, J. Oakley, D.A. Rothamer, R. Bonazza, Phys. Fluids **24**, 074105 (2012)
9. R. Keane, R. Adrian, Appl. Sci. Res. **49**, 191–215 (1992)
10. S. Gerashchenko, K. Prestridge, J. Turbul. **16**, 1011–1035 (2015)